Available online at www.sciencedirect.com
ScienceDirect
Trans. Nonferrous Met. Soc. China 34(2024) 1817−1828
Transactions of Nonferrous Metals Society of China
www.tnmsc.cn

Effect of Gd on preparation of nanocrystalline Mg alloys via cold rotary swaging

Xin CHEN[1], Si-long LI[2], Ying-chun WAN[2]

1. School of Minerals Processing and Bioengineering, Central South University, Changsha 410083, China;
2. Light Alloy Research Institute, Central South University, Changsha 410083, China

Received 13 October 2022; accepted 12 April 2023

Abstract: The effects of Gd element on the nanocrystallization of Mg alloys during swaging were studied by means of the microhardness test, tensile test, and transmission electron microscopy. The results indicate that it is impossible to achieve nanocrystallization in pure Mg via rotary swaging, which may be attributed to the difficulty of forming dislocation arrays. In contrast, adding Gd alone can achieve a remarkable grain refinement effect after swaging. In the early stage of swaging, twin lamellae are all formed in the pure Mg and Mg−Gd alloys. As the swaging process continues, more non-basal dislocations are formed in the Mg−Gd alloys than in pure Mg. This promotes the formation of dislocation arrays and the resulting nanocrystallization in the Mg−Gd alloys. As the Gd content increases, the refinement effect is obviously enhanced. The critical content for the refinement of the grain size below 100 nm is about 5.4 wt.%.

Key words: Mg−Gd alloy; cold rotary swaging; nanocrystallization; twinning; dislocation arrays

1 Introduction

Magnesium (Mg) alloys can exhibit remarkable solid solution strengthening and precipitation strengthening at room temperature and elevated temperature through the appropriate addition of rare earth (RE) elements [1]. Compared with other RE elements, gadolinium (Gd) has a higher solid solubility in α-Mg, and its maximum solubility at the eutectic temperature (821 K) is 23.49 wt.% [2]. Adding Gd results in a great strengthening effect [3] and a high potential to randomize the sheet texture [4] in Mg alloys. Moreover, the addition of Gd can also effectively improve the corrosion resistance [5] and creep resistance [6] of Mg alloys. Owing to the superior properties achieved by the addition of Gd, research on the effect of Gd on the deformation behavior of Mg alloys has attracted increasing attention in recent years. MOUHIB et al [7] found that Mg−Gd−Zn alloys with a lower atomic ratio of Gd to Zn (1∶2) showed a higher direction dependent anisotropy of the yield stress than the higher Gd:Zn atomic ratios (1∶1 and 2∶1). WANG et al [8] reported that Gd could promote the grain refinement of Mg−Gd−Y−Zr alloys during casting.

It is known that basal $\langle a \rangle$ slip dominates the room-temperature plastic deformation of Mg alloys. The addition of Gd reduces the difference in the critical resolved shear stress between the basal $\langle a \rangle$ slip and the pyramidal $\langle c+a \rangle$ slip at room temperature, resulting in an increase in the activity of non-basal slip in Mg alloys [9]. Compared with pure Mg, the addition of Gd promotes the formation of more uniformly distributed shear bands [10], which may be attributed to the activation of more non-basal dislocations in Mg alloys [11]. For twinning, the number density of $\{10\bar{1}2\}$ twins (the

Corresponding author: Ying-chun WAN, Tel: +86-18900706916, E-mail: ycwanmse@csu.edu.cn
DOI: 10.1016/S1003-6326(24)66509-X

most common type of twins in Mg alloys) decreases with increasing Gd content in the α-Mg matrix [12]. Moreover, the addition of Gd can promote the formation of another type of twin, such as $\{11\bar{2}1\}$ twins, which cannot be formed in pure Mg [12]. The addition of Gd also affects the grain refinement process of Mg alloys. It has been reported that among a series of Mg−Gd binary alloys with Gd contents between 0.22 and 4.65 wt.% Gd, a minimum recrystallized grain size was obtained in alloys with 0.75 wt.% Gd [13]. Above this content, the recrystallized grain size increased with increasing Gd content [13]. With the addition of Gd, the refinement mechanism of Mg alloys changed from discontinuous dynamic recrystallization (DRX) to continuous DRX during hot extrusion [14], which was attributed to the formation of solute clusters and the grain boundary segregation of Gd [14,15]. When the Gd content reached 15 wt.%, many fine particles dynamically precipitated along the grain boundaries of Mg−Gd alloys during the hot extrusion process [3], resulting in a finer dynamically recrystallized grain size due to the pinning effect.

To date, most of the research on the effect of Gd on Mg alloys was focused on the hot deformation. There are few studies on its role during cold deformation. Recently, we successfully prepared a bulk nanocrystalline Mg−8Gd−3Y−0.4Zr (wt.%) alloy via rotary swaging at room temperature [16]. However, it is still unclear whether it is possible to achieve nanocrystallization in Mg−Gd binary alloys without adding yttrium (Y). If it can be achieved, what is the correlation between the Gd content and the grain refinement of Mg alloys during swaging? In this work, cold rotary swaging technology was applied to processing Mg−Gd binary alloys and pure Mg. The microstructure evolution of the samples with different Gd addition levels and the effect of Gd in different stages of the grain refinement process were studied.

2 Experimental

2.1 Sample preparation

Three binary alloy compositions containing 1.7, 3.7 and 5.8 wt.% Gd were prepared. These compositions were chosen to be within the range of Gd solid solubility. Each alloy was prepared in an induction furnace under a CO_2 and SF_6 atmosphere and cast in an upright semi-continuous casting machine. The T4 solution treatment was conducted in an air furnace at 798 K for 20 h, followed by air cooling. The solution-treated billets were machined into cylindrical rods with a diameter of 90 mm and a length of 250 mm. Then, backward extrusion was performed at 693 K to produce cylindrical bars with a diameter of 18 mm. The extrusion ratio was 25, and the extrusion rate was 10 mm/s.

For comparison, a commercial hot-extruded pure Mg bar with a diameter of 18 mm was also used as the experimental alloy in this work. The chemical compositions that were determined by inductively coupled plasma mass spectrometry, are listed in Table 1. Figure 1 shows the microstructures of the extruded Mg−1.7Gd, Mg−3.7Gd and Mg−5.8Gd alloys, and pure Mg bars. The average grain sizes are (12±8), (12±5), (13±5), and (19±12) μm, respectively.

Table 1 Chemical compositions of Mg−Gd binary alloys and pure Mg (wt.%)

Material	Gd	Fe	Si	Mn	Ni
Mg−1.7Gd	1.74	0.008	0.019	0.012	0.0003
Mg−3.7Gd	3.65	0.011	0.027	0.017	0.0005
Mg−5.8Gd	5.77	0.014	0.020	0.014	0.0002
Pure Mg		0.006	0.011	0.005	0.0001

The Mg−1.7Gd, Mg−3.7Gd and Mg−5.8Gd alloys, and pure Mg extruded bars were subjected to multi-pass rotary swaging at room temperature without any intermediate annealing. The accumulated strains after different passes calculated from the area reduction $\varphi=\ln(S_0/S_1)$ (S_0: initial cross section, S_1: final cross section), are listed in Table 2. A photo of the extruded and 5-pass swaged alloy bars is shown in Fig. 2.

2.2 Mechanical tests and microstructure characterization

The Vickers microhardness measurement was carried out using an HMV-G 21DT tester with a load of 4.9 N and a dwell time of 15 s. The microhardness for each point was determined by averaging the values from three indentations. An Instron 3369 machine was used to perform tensile tests at room temperature with an initial strain rate of 0.001 s^{-1}. The tensile direction is parallel to the

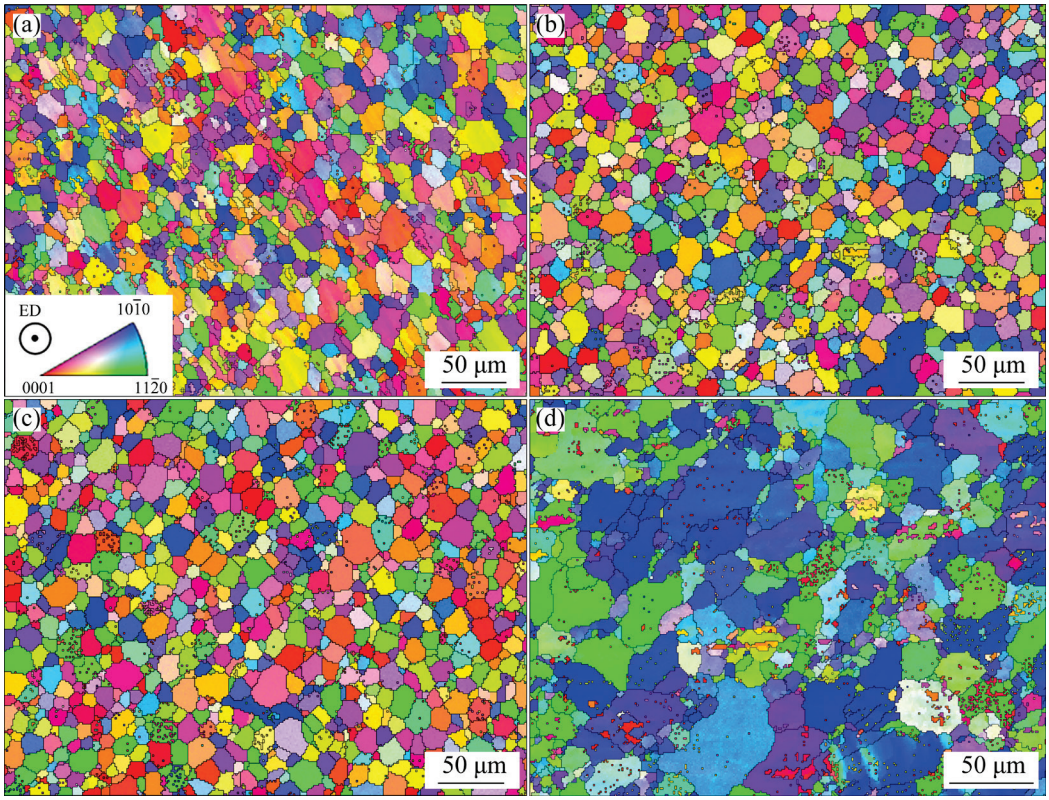

Fig. 1 Microstructures of cross sections of extruded alloy bars: (a) Mg−1.7Gd; (b) Mg−3.7Gd; (c) Mg−5.8Gd; (d) Pure Mg

Table 2 Accumulated strains after different passes

Sample				Swaging pass	Accumulated strain
Mg−1.7Gd-0	Mg−3.7Gd-0	Mg−5.8Gd-0	Pure Mg-0	0	0
Mg−1.7Gd-1	Mg−3.7Gd-1	Mg−5.8Gd-1	Pure Mg-1	1st	0.03
Mg−1.7Gd-2	Mg−3.7Gd-2	Mg−5.8Gd-2	Pure Mg-2	2nd	0.08
Mg−1.7Gd-3	Mg−3.7Gd-3	Mg−5.8Gd-3	Pure Mg-3	3rd	0.14
Mg−1.7Gd-4	Mg−3.7Gd-4	Mg−5.8Gd-4	Pure Mg-4	4th	0.19
Mg−1.7Gd-5	Mg−3.7Gd-5	Mg−5.8Gd-5	Pure Mg-5	5th	0.24

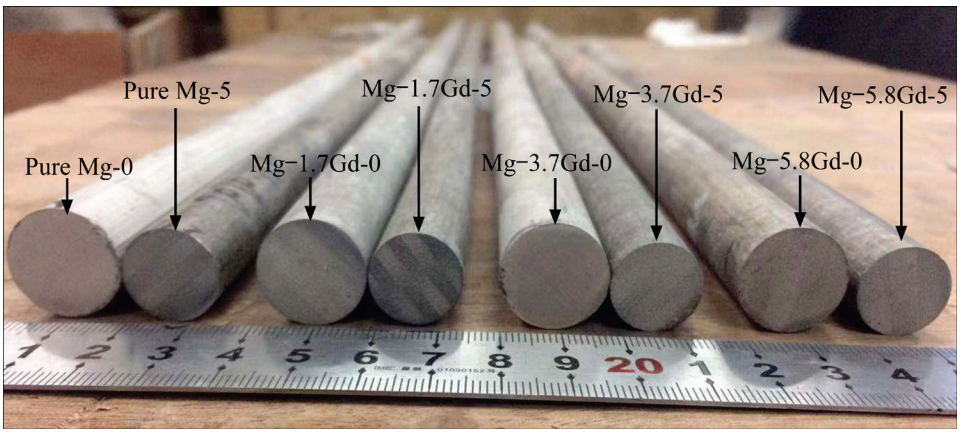

Fig. 2 Photo of extruded and 5-pass swaged alloy bars

ED. All specimens with a gage length of 15 mm and a gage diameter of 3 mm were cut from the center of the alloy bars.

All samples used for the microstructure characterization were cut from the center of the alloy bars and perpendicular to the ED. Electron backscatter diffraction (EBSD) measurements were performed using a Helios Nanolab 600i scanning electron microscope equipped with the HKL Channel 5 data acquisition and analysis software. Transmission electron microscopy (TEM) and high-resolution TEM (HRTEM) observations were conducted on a Titan G^2 60−300 microscope operating at 300 kV. The TEM samples were mechanically ground to a thickness of 100 μm, and then thinned by twin-jet electropolishing in an electrolyte containing 1 vol.% nitric acid, 2 vol.% perchloric acid, and 97 vol.% ethanol. The electropolishing temperature was approximately −40 °C. The average grain or subgrain size was measured by the Nano Measurer software. At least 500 grains or subgrains were measured for the statistical analysis.

3 Results

Our previous work [16] indicated that bulk nanocrystalline Mg alloys with dimensions of *d*3 mm × 1000 mm were obtained by rotary swaging at room temperature. Nanocrystallization was achieved in the central region of the alloy bars rather than in the edge region, due to the unique loading mode and the high hydrostatic stress in the central region. Therefore, all mechanical tests and microstructure characterization in this study were focused on the central region of the alloy bars.

3.1 Microhardness at center of alloy bars

Figure 3(a) shows the variation in the hardness with the increase in the number of swaging pass. Compared with the extruded samples, the pure Mg-5 sample shows only a small increment (approximately HV 6) in the microhardness in the central region. In contrast, the microhardness values of the Mg−1.7Gd-5, Mg−3.7Gd-5 and Mg−5.8Gd-5 samples increase significantly by approximately HV 26, HV 33 and HV 37, respectively, as shown in Fig. 3(b). The increment in microhardness of the Gd-containing alloys after 5-pass swaging compared to the extruded samples gradually increases with increasing Gd content.

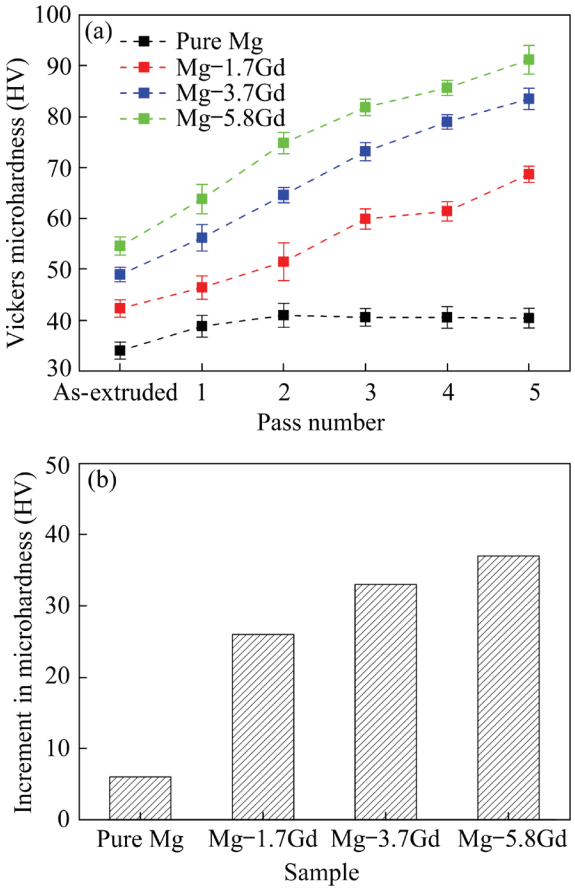

Fig. 3 Microhardness of pure Mg and Mg−Gd alloys after different swaging passes (a), and increment in microhardness between 5-pass swaging and extruded samples (b)

3.2 Microstructure evolution during swaging

3.2.1 Formation of twin lamellae and deformation bands

Figures 4(a−c) show the typical microstructures of the Mg−1.7Gd-1, Mg−3.7Gd-1 and Mg−5.8Gd-1 samples, respectively. After 1-pass swaging, many lamellae were formed in the three samples. Based on the random selected-area electron diffraction (SAED) analysis of ten lamellae, most of them are determined to be $\{10\bar{1}2\}$ tension twins, as shown in the insets in Figs. 4(a−c). The average width of the twin lamellae in the three samples ranges from 300 to 400 nm. Within the twin lamellae and the adjacent matrix, many basal stacking faults (SFs, white arrows) can be observed, especially in the Mg−5.8Gd-1 sample, as shown in Figs. 4(d) and (e).

Apart from the twin lamellae, some deformation bands were also observed in the Mg−5.8Gd alloy bar in the early stage of swaging.

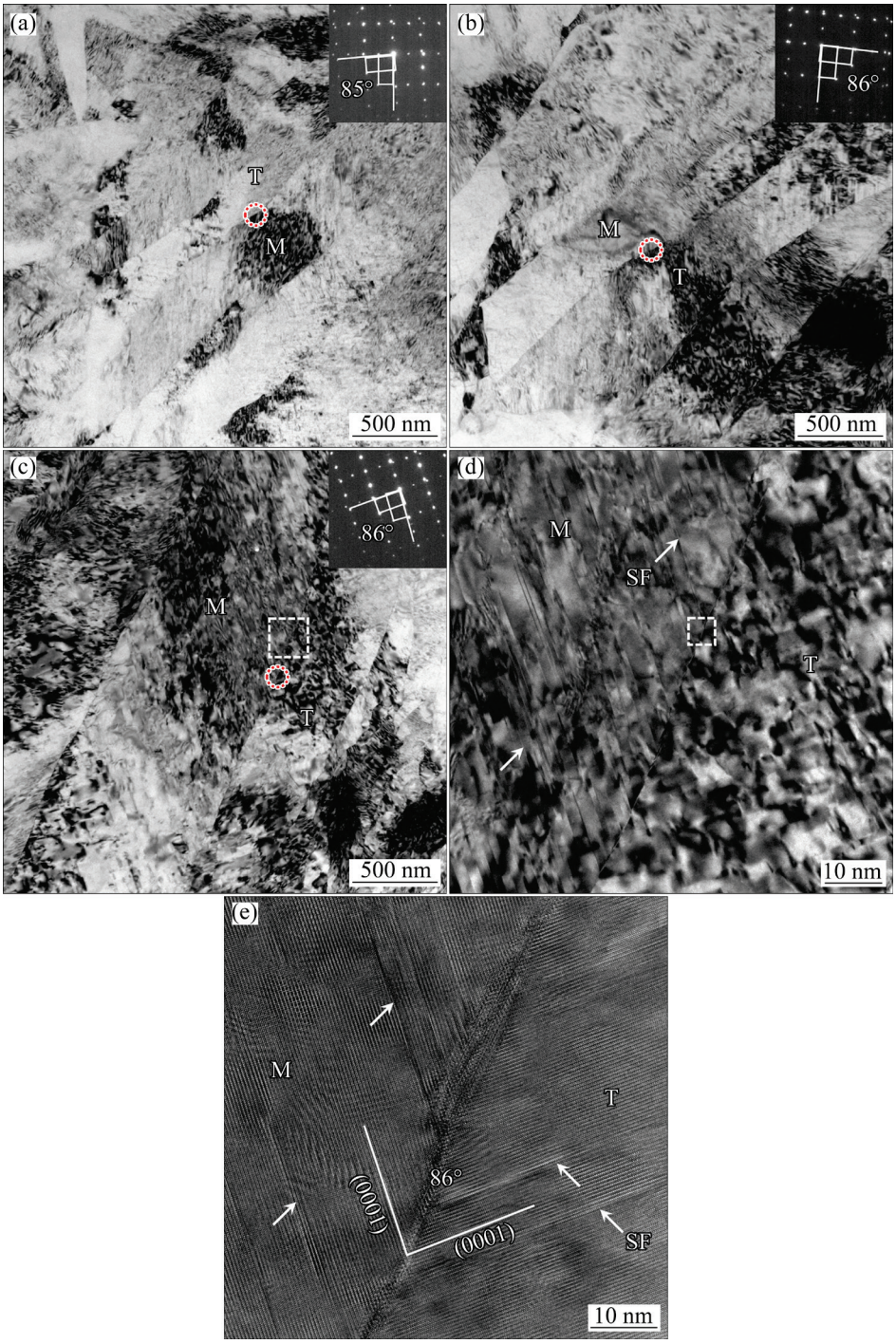

Fig. 4 Typical microstructures after 1-pass swaging: (a) Mg−1.7Gd-1; (b) Mg−3.7Gd-1; (c) Mg−5.8Gd-1; (d) Magnified TEM image of white dotted box in (c), showing many SFs (white arrows) formed in matrix (labeled "M") and twin (labeled "T"); (e) Magnified HRTEM image of white dotted box in (d) (The corresponding SAED patterns of the twin boundary area (red circle) are provided as insets in the photomicrograph)

Figure 5(a) shows some deformation bands with width ranging from 200 to 300 nm formed in the Mg−5.8Gd-2 sample. Basal SFs can also be observed within the bands and the adjacent matrix. As shown in Fig. 5(b), the boundary of the deformation band exhibits a high misorientation angle of approximately 11° with its adjacent matrix. It is worth noting that these deformation bands were not observed in the Mg−1.7Gd and Mg−3.7Gd samples during swaging.

3.2.2 Further refinement by forming dislocation arrays

As the swaging strain increased, the twin lamellae and deformation bands that formed in the

early stage of swaging were further refined through the formation of dislocation arrays. One of the dislocation arrays (red arrows) that formed within the twin lamellae in the Mg−1.7Gd-3 sample is presented in Fig. 6(a). The magnified HRTEM image of the dislocation array in Fig. 6(b) shows the low-angle grain boundary (LAGB) formed by the dislocation array. Figures 6(c) and (d) show the

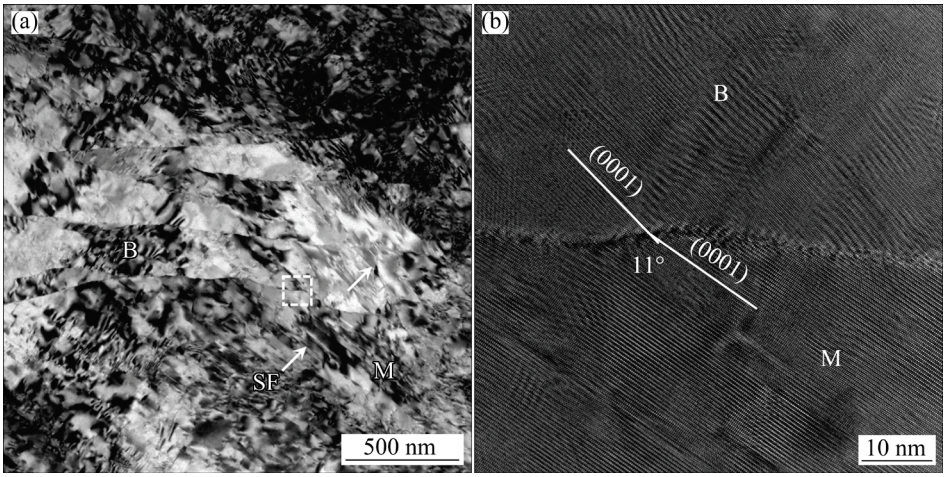

Fig. 5 (a) Deformation bands (labeled "B") observed in central region of Mg−5.8Gd alloy bar after 2-pass swaging; (b) Magnified HRTEM image of white dotted box in (a)

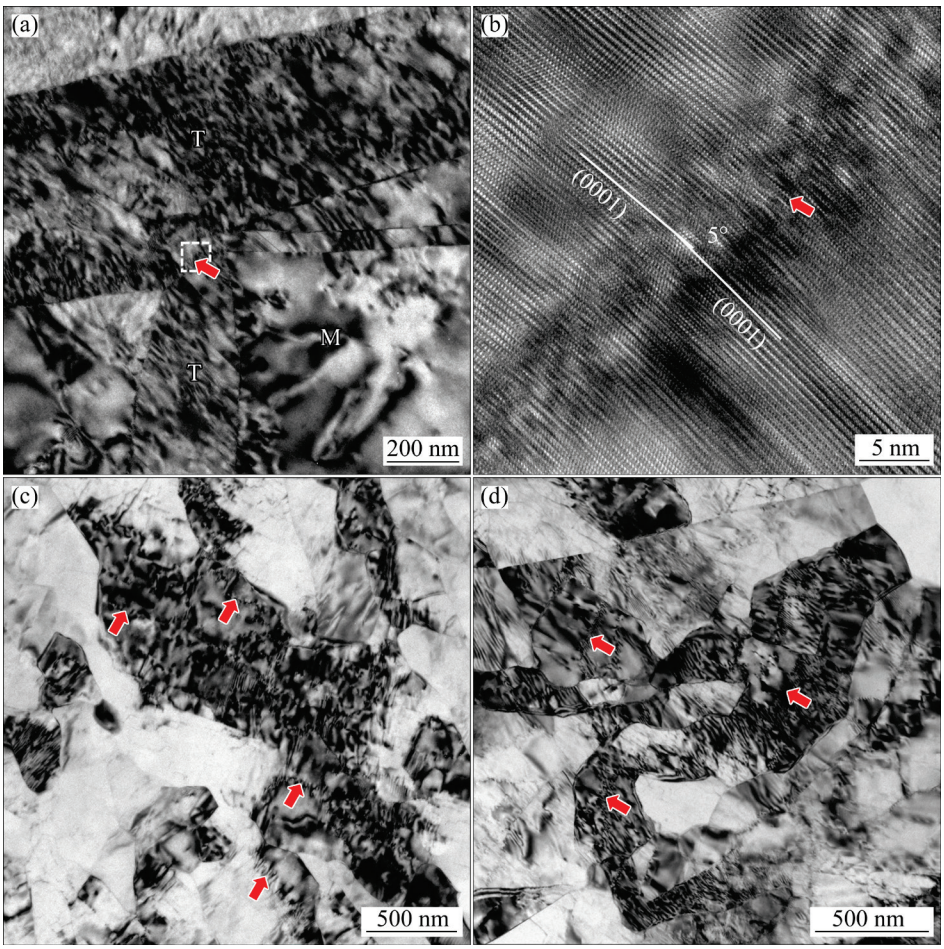

Fig. 6 (a) Further refinement of twin lamellae through formation of dislocation arrays (red arrow) in Mg−1.7Gd-3 sample; (b) Magnified HRTEM image of white dotted box in (a), showing 5° LAGB formed by dislocation array; (c, d) Formation of nanoscale submicrostructures through segmentation by dislocation arrays in Mg−3.7Gd-3 and Mg−5.8Gd-3 samples, respectively

nanoscale submicrostructure formed through segmentation by the dislocation arrays in Mg−3.7Gd-3 and Mg−5.8Gd-3 samples, respectively. With continued increase in the swaging strain, due to the increase in dislocation accumulation, these dislocation arrays could be transformed into subgrain boundaries [17]. A nanoscale subgrain that formed in the Mg−5.8Gd-4 sample is presented in Fig. 7, showing 10° and 15° crystal misorientations with its neighboring grains. These nanoscale subgrains would be further transformed into nanograins with high-angle grain boundaries (HAGB) through more dislocation accumulation and interaction within the boundaries and subsequent crystal rotation with their neighboring grains [18].

3.2.3 Comparison of microstructures after same 5-pass swaging

After the same 5-pass swaging, remarkable grain refinement (green arrows) could be achieved in the Mg−1.7Gd-5, Mg−3.7Gd-5 and Mg−5.8Gd-5 samples, as shown in Figs. 8(a−c), respectively. The average grain/subgrain sizes of the Mg−1.7Gd-5, Mg−3.7Gd-5 and Mg−5.8Gd-5 samples are approximately 298, 180 and 87 nm, respectively. It is worth noting that some fine lamellae (yellow arrows) were still observed without further refinement. In contrast, only twin lamellae were observed in the pure Mg-5 sample, and no dislocation arrays were found within the twin lamellae or in the matrix, as shown in Fig. 8(d).

3.3 Improvement in strength via rotary swaging

Figure 9(a) shows the room-temperature tensile stress−strain curves of the samples after extrusion and the same 5-pass swaging. The corresponding mechanical properties are listed in Table 3. The three groups of Mg−Gd samples all exhibit significant increase in yield and ultimate strength after 5-pass swaging. Compared with the

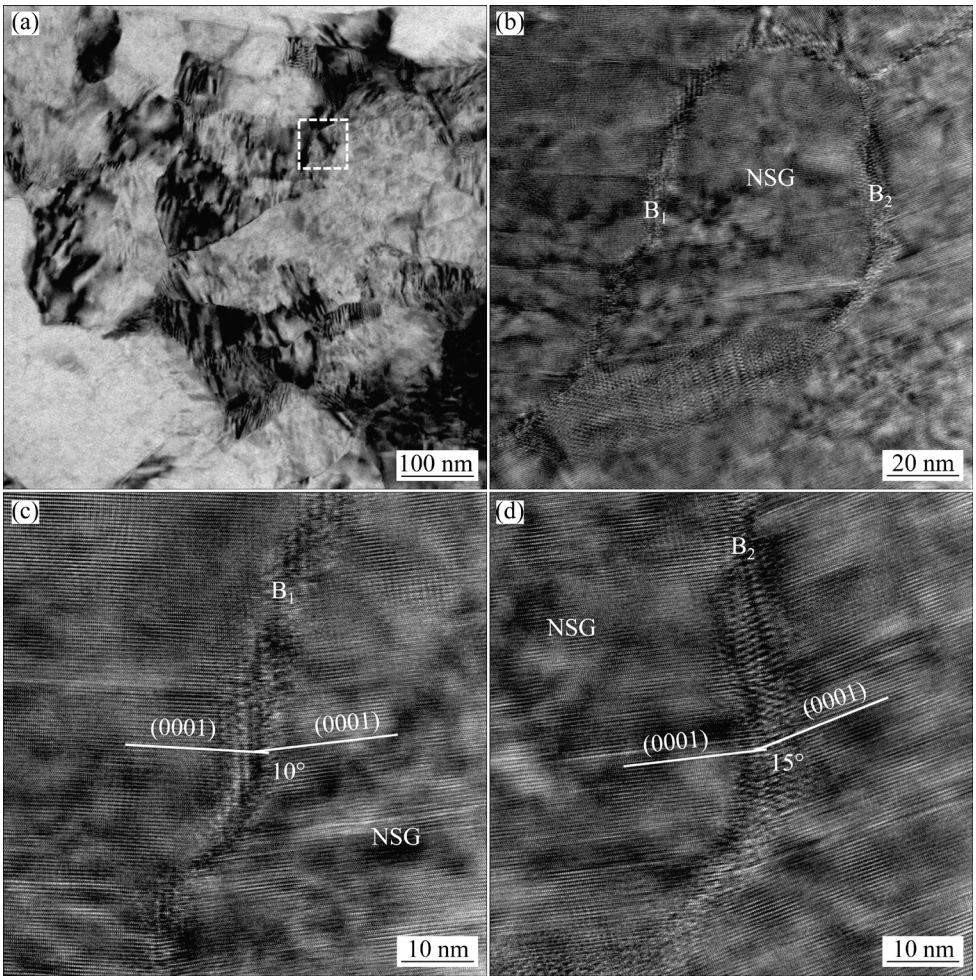

Fig. 7 (a) Microstructure observed in Mg−5.8Gd-4 sample; (b) Magnified HRTEM image of white dotted box in (a), showing nanoscale subgrain (labeled "NSG") with size of ~40 nm; (c, d) HRTEM images of grain boundaries marked B_1 and B_2 in (b), respectively

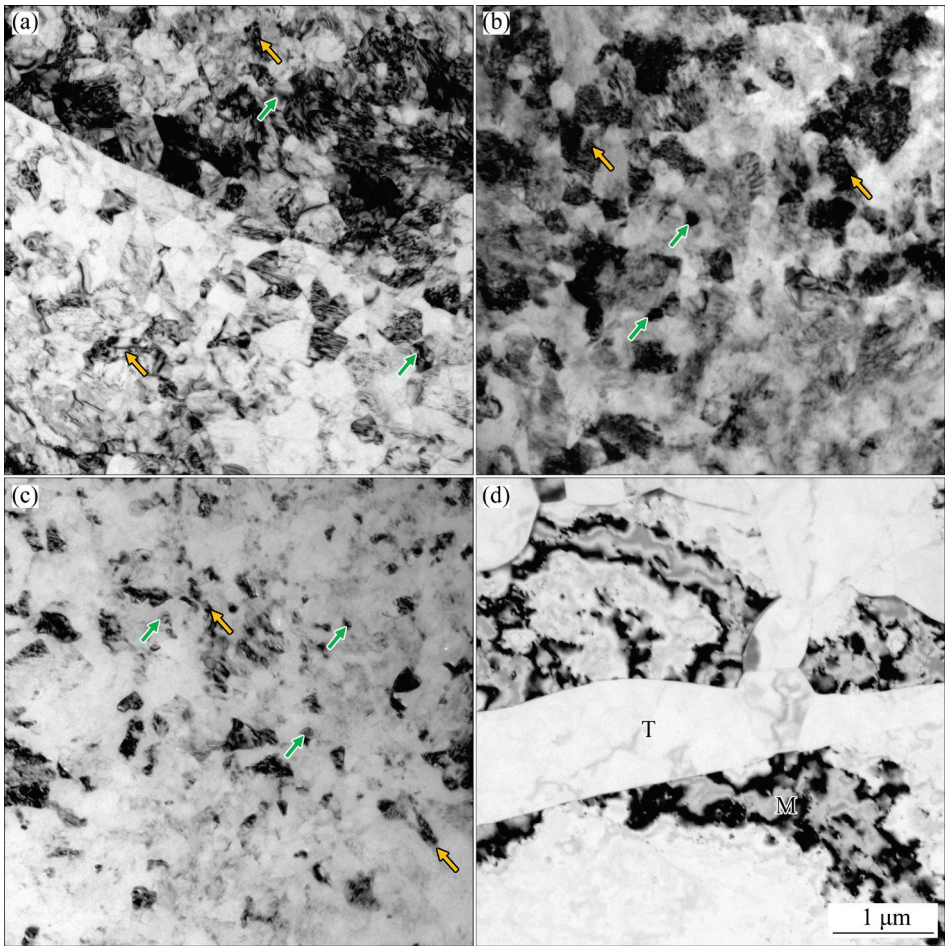

Fig. 8 Typical microstructures observed after 5-pass swaging: (a) Mg−1.7Gd-5; (b) Mg−3.7Gd-5; (c) Mg−5.8Gd-5; (d) Pure Mg (Nanoscale grains (or subgrains) and lamellae are indicated by the green and yellow arrows in the images, respectively)

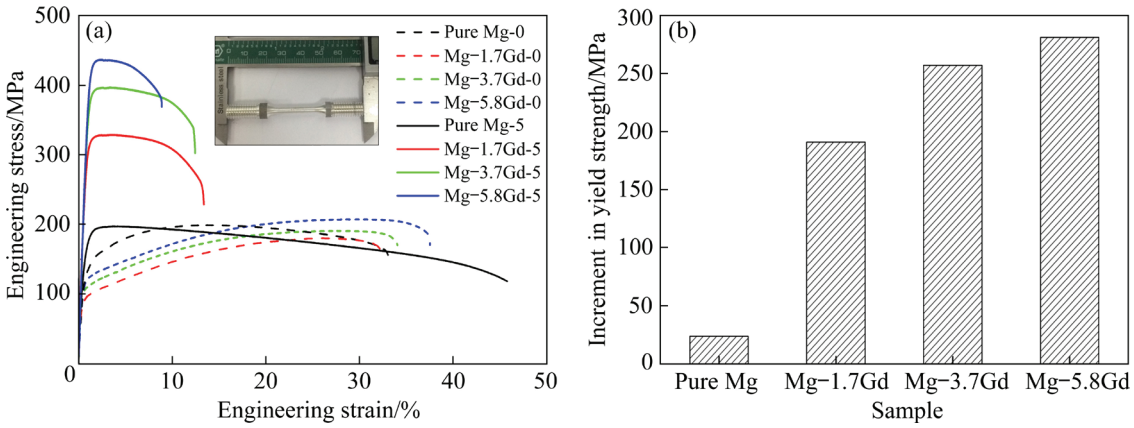

Fig. 9 (a) Room-temperature tensile stress−strain curves of extruded and swaged samples; (b) Increment in yield strength between 5-pass swaging and extruded samples

extruded samples, the increment in yield strength after 5-pass swaging increases with increasing Gd addition. As shown in Fig. 9(b), the increment in the yield strength of the Mg−1.7Gd, Mg−3.7Gd and Mg−5.8Gd samples after 5-pass swaging are 191, 257 and 281 MPa, respectively. In contrast, the yield strength of the pure Mg sample increases only slightly (24 MPa) after the same 5-pass swaging.

Table 3 Yield strength (YS), ultimate tensile strength (UTS) and elongation at fracture (ε_{ef}) of extruded and swaged samples

Sample	YS/MPa	UTS/MPa	ε_{ef}/%
Pure Mg-0	106	199	33.1
Pure Mg-5	130	198	45.8
Mg−1.7Gd-0	82	180	32.6
Mg−1.7Gd-5	273	329	13.4
Mg−3.7Gd-0	98	191	34.2
Mg−3.7Gd-5	355	397	12.4
Mg−5.8Gd-0	107	207	37.5
Mg−5.8Gd-5	388	437	8.9

4 Discussion

4.1 Effect of Gd addition on activity of non-basal slip

Unlike Mg−Gd binary alloys, pure Mg cannot develop nanocrystallization via current rotary swaging technology. Our previous work [16] has shown that dislocation arrays are an indispensable factor in the nanocrystallization of Mg alloys during swaging. In this work, no dislocation arrays were found in the swaged pure Mg samples. Figures 10(a, b) show the TEM dark field observations of the pure Mg and Mg−1.7Gd samples after 1-pass swaging, respectively. Based on the $g\cdot b$ criterion, the visible dislocations with g=(0002) under dark field conditions have a $\langle c\rangle$ component, which are typical non-basal dislocations ($\langle c\rangle$ or $\langle c+a\rangle$ dislocations) in Mg. In the pure Mg sample, few non-basal dislocations are observed, as shown in Fig. 10(a). Studies indicate that non-basal dislocations in pure Mg are unstable and easily dissociate within the basal plane at room temperature [19,20]. The dislocation arrays in Mg alloys mainly originate from the accumulation and interaction of non-basal dislocations [21,22]. The low density of non-basal dislocations makes it difficult for pure Mg to form dislocation arrays during swaging. In contrast, numerous non-basal dislocations with $\langle c\rangle$ components are observed in the Mg−1.7Gd sample after 1-pass swaging, as shown in Fig. 10(b). Compared with pure Mg, the higher activity of non-basal slips in Mg−Gd binary alloys can be attributed to the inhibition of dissociation of non-basal dislocations to the basal plane, which is due to the addition of Gd and rapid non-basal dislocation multiplication through solute-accelerated cross-slip and double cross-slip [23]. This promotes the formation of more dislocation arrays and the resulting nanocrystallization in the Mg−Gd binary alloys during swaging.

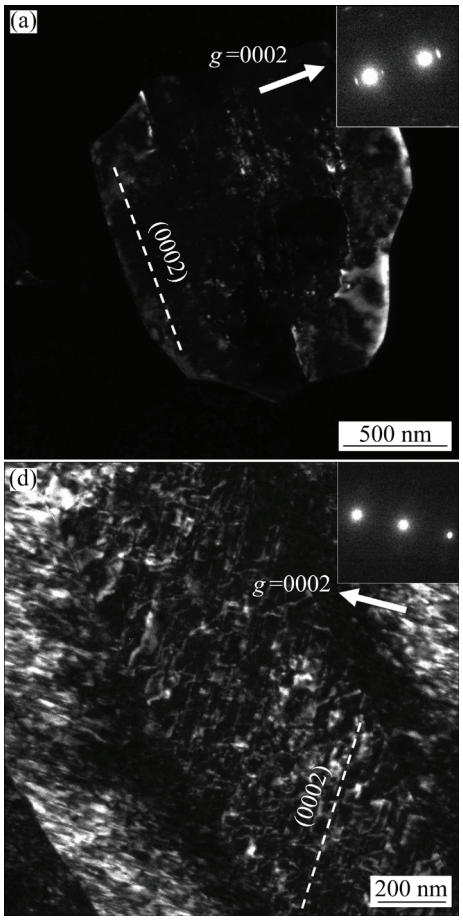

Fig. 10 TEM dark field images of pure Mg-1 (a), and Mg−1.7Gd-1 (b)

4.2 Effect of Gd addition on nanocrystallization process

After 5-pass swaging, a finer grain/subgrain size was obtained in the Mg−Gd binary alloys with more Gd addition, as shown in Fig. 8. Figure 11 shows the relationship between the final grain/subgrain size after 5-pass swaging and the Gd content based on the statistical analysis. The Gd content is estimated to be inversely proportional to the final grain/subgrain size, and the critical Gd addition amount for refining grains below 100 nm (a typical size of nanocrystalline materials) is estimated to be about 5.4 wt.% based on the linear fitting of data. The above TEM observations indicate that the nanocrystallization process of Mg−Gd binary alloys mainly depends on the formation of twin lamellae/deformation bands at the beginning

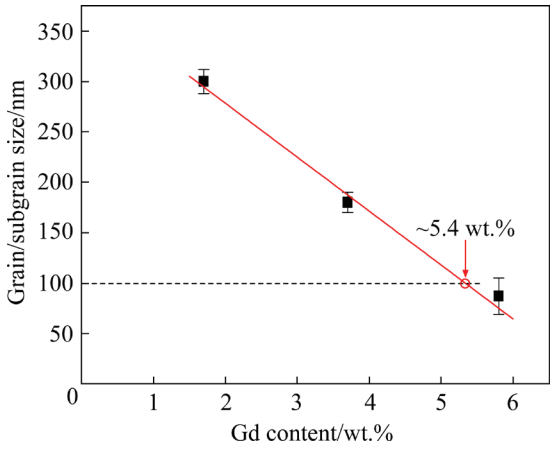

Fig. 11 Relationship between Gd content and grain/subgrain size in Mg−Gd binary alloys after 5-pass swaging

and subsequent dislocation arrays. In different stages, the effect of Gd addition is different.

In the early stage of swaging, $\{10\bar{1}2\}$ tension twinning dominated the refinement process in the Mg−Gd binary alloys. The widths of the twin lamellae among the three groups of Mg−Gd samples were similar, as shown in Fig. 4. This indicates that the thickness of the initial tension twins formed is independent of the Gd content and may be dependent on the strain rate during high-strain swaging (approximately 50 s^{-1} in the present work) [24]. In addition to twinning, some deformation bands also formed in the Mg−5.8Gd sample, which were not observed in the Mg−1.7Gd and Mg−3.7Gd samples, as shown in Fig. 5. The main reason is that non-basal slips in the sample with more Gd addition have a higher activity, resulting in a lower twinning activity. Therefore, it produced another deformation mode, that is, deformation bands formed to adapt to the local stress concentration during swaging. However, it is worth noting that only a small number of deformation bands were observed in the Mg−5.8Gd sample. This should not be the main reason for the different grain/subgrain sizes obtained by different Gd additions.

As the swaging process continued, the formation of dislocation arrays dominated the further refinement of the twin lamellae and the deformation bands. As discussed in Section 4.1, adding more Gd to Mg alloys could more effectively inhibit the dissociation of non-basal dislocations and promote the formation of more non-basal dislocations. Logically, the higher activity of non-basal slip further promotes the formation of more dislocation arrays in the Mg−Gd binary alloys. Therefore, a finer submicrostructure could be obtained through segmentation by more dislocation arrays, which resulted in a finer grain/subgrain size in the Mg alloys with increasing Gd content.

5 Conclusions

(1) Adding Gd to α-Mg alone can achieve a significant grain refinement via rotary swaging, resulting in the significant improvement in microhardness and strength. After the same 5-pass swaging, the increments in yield strength of the Mg−1.7Gd, Mg−3.7Gd, and Mg−5.8Gd alloys are 191, 257 and 281 MPa, respectively, showing the much higher increment than that of pure Mg (24 MPa).

(2) Dislocation arrays have not been observed within the lamellae or in the matrix of the pure Mg. The difficulty in forming dislocation arrays is attributed to the much lower activity of non-basal slips in the pure Mg during swaging.

(3) The nanocrystallization process in the Mg−Gd alloys includes the dominant twinning process first, and further refinement through forming massive dislocation arrays.

(4) The grain refinement effect after swaging is obviously enhanced with increasing Gd content in α-Mg. The average grain/subgrain sizes of the Mg−1.7Gd, Mg−3.7Gd and Mg−5.8Gd alloys after 5-pass swaging are approximately 298, 180 and 87 nm, respectively. The critical content of Gd addition for the refinement of the grain size below 100 nm in Mg−Gd binary alloys is estimated to be about 5.4 wt.%.

CRediT authorship contribution statement

Xin CHEN: Conceptualization, Methodology, Writing − Original draft preparation; **Si-long LI:** Supervision; **Ying-chun WAN:** Writing − Review & Editing.

Declaration of competing interest

The authors declare that they have no known competing financial interests or personal relationships that could have appeared to influence the work reported in this paper.

Acknowledgments

This work was supported by the National Natural Science Foundation of China (No. 52204409).

References

[1] CAO Fu-yong, ZHANG Jing, LI Ke-ke, SONG Guang-ling. Influence of heat treatment on corrosion behavior of hot rolled Mg5Gd alloys [J]. Transactions of Nonferrous Metals Society of China, 2021, 31: 939−951.

[2] NIE Jian-feng. Precipitation and hardening in magnesium alloys [J]. Metallurgical and Materials Transactions A, 2012, 43: 3891−3939.

[3] KIM S H, JUNG J G, YOU B S, PARK S H. Microstructure and texture variation with Gd addition in extruded magnesium [J]. Journal of Alloys and Compounds, 2017, 695: 344−350.

[4] AL-SAMMAN T, LI X. Sheet texture modification in magnesium-based alloys by selective rare earth alloying [J]. Materials Science and Engineering A, 2011, 528: 3809−3822.

[5] SUN Yue-hua, WANG Ri-chu, PENG Chao-qun, WANG Xiao-feng. Effect of Gd on microstructure, mechanical properties, and corrosion behavior of as-homogenized Mg−8Li−3Al−2Zn−0.2Zr alloy [J]. Transactions of Nonferrous Metals Society of China, 2022, 32: 2494−2509.

[6] ASHRAFIZADEH S M, MAHMUDI R, GERANMAYEH A R. A comparative study on the effects of Gd, Y and La rare-earth elements on the microstructure and creep behavior of AZ81 Mg alloy [J]. Materials Science and Engineering A, 2020, 790: 139712.

[7] MOUHIB F, PEI R, EROL B, SHENG F, KORTE-KERZEL S, AL-SAMMAN T. Synergistic effects of solutes on active deformation modes, grain boundary segregation and texture evolution in Mg−Gd−Zn alloys [J]. Materials Science and Engineering A, 2022, 847: 143348.

[8] WANG Xue-zhao, WANG You-qiang, NI Chen-bing, FANG Yu-xin, YU Xiao, ZHANG Ping. Effect of Gd content on microstructure and dynamic mechanical properties of solution-treated Mg−*x*Gd−3Y−0.5Zr alloy [J]. Transactions of Nonferrous Metals Society of China, 2022, 32: 2177−2189.

[9] XU C, NAKATA T, QIAO X G, ZHENG M Y, WU K, KAMADO S. Ageing behavior of extruded Mg−8.2Gd−3.8Y−1.0Zn−0.4Zr (wt.%) alloy containing LPSO phase and γ' precipitates [J]. Scientific Reports, 2017, 7: 43391.

[10] STANFORD N, BARNETT M R. The origin of "rare earth" texture development in extruded Mg-based alloys and its effect on tensile ductility [J]. Materials Science and Engineering A, 2008, 496: 399−408.

[11] LEE S W, KIM S H, JO W K, HONG W H, KIM W, MOON B G, PARK S H. Twinning and slip behaviors and microstructural evolutions of extruded Mg−1Gd alloy with rare-earth texture during tensile deformation [J]. Journal of Alloys and Compounds, 2019, 791: 700−710.

[12] HE Cong, LI Zhi-qiao, KONG De-hao, ZHAO Xiao-jun, CHEN Hou-wen, NIE Jian-feng. Origin of profuse $\{11\bar{2}1\}$ deformation twins in Mg−Gd alloys [J]. Scripta Materialia, 2021, 191: 62−66.

[13] STANFORD N, ATWELL D, BARNETT M R. The effect of Gd on the recrystallisation, texture and deformation behaviour of magnesium-based alloys [J]. Acta Materialia, 2010, 58: 6773−6783.

[14] HADORN J P, SASAKI T T, NAKATA T, OHKUBO T, KAMADO S, HONO K. Solute clustering and grain boundary segregation in extruded dilute Mg−Gd alloys [J]. Scripta Materialia, 2014, 93: 28−31.

[15] BASU I, PRADEEP K G, MIEβEN C, BARRALES-MORA L A, AL-SAMMAN T. The role of atomic scale segregation in designing highly ductile magnesium alloys [J]. Acta Materialia, 2016, 116: 77−94.

[16] WAN Ying-chun, TANG Bei, GAO Yong-hao, TANG Ling-ling, SHA Gang, ZHANG Bo, LIANG Ning-ning, LIU Chu-ming, JIANG Shu-nong, CHEN Zhi-yong, GUO Xue-yi, ZHAO Yong-hao. Bulk nanocrystalline high-strength magnesium alloys prepared via rotary swaging [J]. Acta Materialia, 2020, 200: 274−286.

[17] SUN H Q, SHI Y N, ZHANG M X, LU K. Plastic strain-induced grain refinement in the nanometer scale in a Mg alloy [J]. Acta Materialia, 2007, 55: 975−982.

[18] GAO Jun-jie, FU Jie, ZHANG Nan, CHEN Yu-an. Structural features and mechanical properties of Mg−Y−Zn−Sn alloys with varied LPSO phases [J]. Journal of Alloys and Compounds, 2018, 768: 1029−1038.

[19] WU Zhao-xuan, CURTIN W A. The origins of high hardening and low ductility in magnesium [J]. Nature, 2015, 526: 62−67.

[20] WU Zhao-xuan, AHMAD R, YIN Bing-lun, SANDLÖBES S, CURTIN W A. Mechanistic origin and prediction of enhanced ductility in magnesium alloys [J]. Science, 2018, 359: 447−452.

[21] LI B, MA E, RAMESH K T. Dislocation configurations in an extruded ZK60 magnesium alloy [J]. Metallurgical and Materials Transactions A, 2008, 39: 2607−2614.

[22] WANG Bi-zheng, TANG Bei, YOU Chao, WAN Ying-chun, GAO Yong-hao, CHEN Zhi-yong, LU Li-wei, LIU Chu-ming, WANG Jian. Dislocation arrays, precipitate bands and free zones in forged Mg−Gd−Y−Zr alloy [J]. Materials Science and Engineering A, 2020, 775: 138789.

[23] AHMAD R, YIN Bing-lun, WU Zhao-xuan, CURTIN W A. Designing high ductility in magnesium alloys [J]. Acta Materialia, 2019, 172: 161−184.

[24] CHEN Xin, LIU Chu-ming, WAN Ying-chun, JIANG Shu-nong, CHEN Zhi-yong, ZHAO Yong-hao. Grain refinement mechanisms in gradient nanostructured AZ31B Mg alloy prepared via rotary swaging [J]. Metallurgical and Materials Transactions A, 2021, 52: 4053−4065.

Gd 对冷旋锻制备纳米晶镁合金的影响

陈 鑫[1]，李思珑[2]，万迎春[2]

1. 中南大学 资源加工与生物工程学院，长沙 410083；
2. 中南大学 轻合金研究院，长沙 410083

摘 要：通过显微硬度测试、拉伸试验和透射电镜手段研究 Gd 元素对冷旋锻过程镁合金纳米化的影响。结果表明，由于纯镁中很难形成位错阵列，旋锻不能实现纯镁纳米化。相比之下，单独添加 Gd，旋锻后镁合金晶粒可得到显著细化。在旋锻早期阶段，纯镁和 Mg−Gd 合金中都形成孪晶片层。随着增加旋锻变形的继续，相比纯镁，更多的非基面位错在 Mg−Gd 合金中形成，这促进了 Mg−Gd 合金中位错阵列的形成，导致合金纳米化。随着 Gd 含量的增加，Mg−Gd 合金晶粒细化效果显著提升，晶粒细化至 100 nm 以下的临界 Gd 含量约为 5.4%(质量分数)。

关键词：Mg−Gd 合金；冷旋锻；纳米化；孪生；位错阵列

(Edited by Xiang-qun LI)